Layer-by-Layer Assembly of Charged Nanoparticles on Porous Substrates: Molecular Dynamics Simulations

Jan-Michael Y. Carrillo and Andrey V. Dobrynin*

Polymer Program, Institute of Materials Science and Department of Physics, University of Connecticut, Storrs, Connecticut 06269, United States

ABSTRACT We performed molecular dynamics simulations of a multilayer assembly of oppositely charged nanoparticles on porous substrates with cylindrical pores. The film was constructed by sequential adsorption of oppositely charged nanoparticles in layer-by-layer fashion from dilute solutions. The multilayer assembly proceeds through surface overcharging after completion of each deposition step. There is almost linear growth in the surface coverage and film thickness during the deposition process. The multilayer assembly also occurs inside cylindrical pores. The adsorption of nanoparticles inside pores is hindered by the electrostatic interactions of newly adsorbing nanoparticles with the multilayer film forming inside the pores and on the substrate. This is manifested in the saturation of the average thickness of the nanoparticle layers formed on the pore walls with an increasing number of deposition steps. The distribution of nanoparticles inside the cylindrical pore was nonuniform with a significant excess of nanoparticles at the pore entrance.

KEYWORDS: computer simulations · layer-by-layer assembly · porous substrates · charged nanoparticles · polyelectrolytes

INTRODUCTION

The layer-by-layer (L-b-L) deposition of charged molecules is a simple and reliable self-assembly technique.[1−9] The key to a successful deposition of multilayer assemblies in a layer-by-layer fashion is the inversion and subsequent reconstruction of the surface properties. This is achieved by immersing a substrate into a dilute aqueous solution of anionic (or cationic) polyelectrolytes for a period of time required for the adsorption of a layer of desired thickness after which the substrate is rinsed. During the next step, a substrate covered with adsorbed polyelectrolytes is exposed to a dilute solution of cationic (or anionic) macromolecules, followed by a rinsing step to obtain an irreversibly adsorbed layer. After just several dipping cycles experiments show a linear increase of the film thickness, indicating that the system has reached a steady state regime. The simplicity of the electrostatic self-assembly technique allows fabrication of multilayer films from synthetic polyelectrolytes, DNA, proteins, nanoparticles, and viruses.[1,2,4−6,9] The multilayer assembly process can be accelerated by utilizing spraying,[9−12] spin-coating,[9,13,14] or printing techniques.[15] These methods have another advantage over the conventional dipping procedure since only small amounts of the solution are needed to cover large surface areas.

Computer simulations[16−26] and theoretical studies[13,27−32] were instrumental in understanding mechanisms and in model progression of the multilayer assembly of oppositely charged polyelectrolytes. Simulations[16−19,23−26,33,34] confirmed that the layer assembly proceeds through surface overcharging during each deposition step and that the film buildup follows a linear growth with both the layer thickness and the surface coverage increasing linearly with the number of deposition steps. This steady state (linear growth) regime is observed in experiments after deposition of the first few layers. The surface roughness and film porosity depends on the rigidity of the adsorbing species.[20] The simulations also showed that multilayer assembly is a nonequilibrium process.[19,26] Given sufficient time, the polyelectrolyte chains preferentially desorb in pairs forming a neutral polyelectrolyte complex in a solution.[19] This optimizes the energy of the electrostatic interactions for chains in solution as compared with those in an L-b-L film. Note that one can also observe a complete layer detachment in a particular range of the interaction parameters.[26]

Recently, there was a substantial interest in porous substrates as templates for the preparation of nanostructured materials with functional hierarchic structures that combined the precise pore geometry and the organized layered structure of an L-b-L assembly.[35−44] Such substrates were used for selective DNA separation and for the development of biosensors and multifunctional

* Address correspondence to avd@ims.uconn.edu.

Received for review January 6, 2011 and accepted March 26, 2011.

Published online March 26, 2011
10.1021/nn200065q

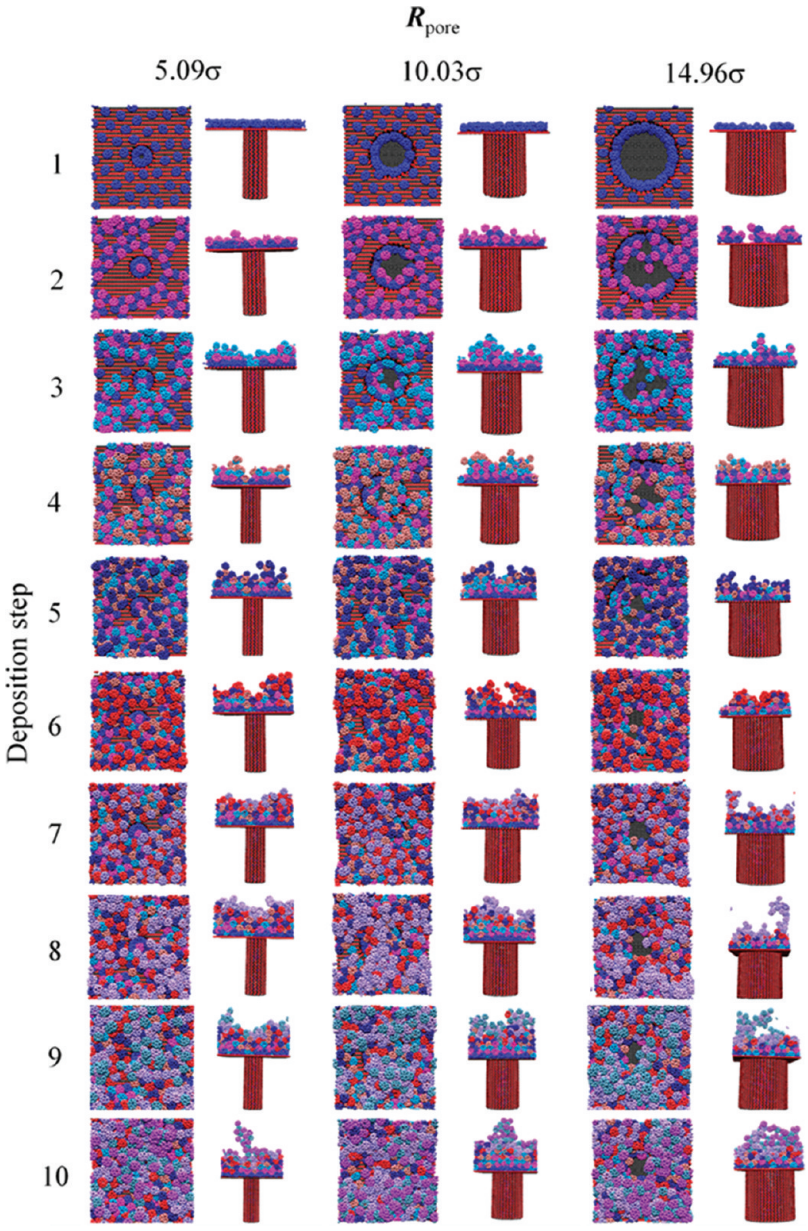

Figure 1. Evolution of the multilayer assembly at charged surfaces. Snapshots are taken after completion of the deposition steps 1 through 10. The positively charged beads of the substrate are shown in red and neutral beads are colored in black. The nanoparticles deposited on the substrate during different deposition steps are colored in blue (1), magenta (2), dodger blue (3), chestnut (4), dark blue (5), dark red (6), slate blue (7), lavender (8), steel blue (9), and purple (10).

substrates (see ref 35 for a review). The selectivity of these substrates is strongly influenced by the pore sizes. The L-b-L assembly technique can be used to control the pore size and selectivity of such substrates (for example, by performing several deposition steps one can initiate a multilayer film growth inside a pore reducing its size). The efficiency of this process depends on the size of the adsorbing macromolecular species, the pore size, and the strength of the electrostatic attraction between porous substrate and polyelectrolytes controlled by the solution ionic strength and pH. Note that overcharging of the L-b-L film inside the pores could lead to electrostatic induced hindrance of the polyelectrolyte diffusion inside the pore. In some cases the electrostatic barrier at the pore entrance can completely inhibit L-b-L assembly, resulting in saturation of the L-b-L layer thickness inside a pore after just few deposition steps.[39] While there are a number of experimental studies of the L-b-L assembly on porous substrates,[35−44] our understanding of the mechanism of the L-b-L growth on such substrates is lagging behind. To address this problem we performed molecular dynamics simulations of the sequential adsorption of oppositely charged nanoparticles on charged substrates with cylindrical pores of different sizes.

RESULTS AND DISCUSSION

Molecular Dynamics Simulations. We have performed molecular dynamics simulations of the L-b-L assembly

of charged nanoparticles on charged substrates with cylindrical pores (see Figure 1). In our simulations we used a coarse-grained representation of nanoparticles, counterions, and substrate (see the section Model and Simulation Details). In this representation monomers belonging to nanoparticles, small ions, and substrate particles are modeled by Lennard-Jones particles (beads) with diameter σ. Nanoparticles consisted of 32 charged monomers (beads) and had C32 fullerene-like structures with diameter 4σ. The structure of nanoparticles was maintained by imposing the FENE and angular potentials on bonds connecting 32 beads belonging to nanoparticles. The substrate was modeled by hexagonally packed lattice of beads. Every second bead on a substrate was charged. We performed simulations of the L-b-L assembly of charged nanoparticles on substrates with cylindrical pores and with radii equal to $R_{pore} = 5.08\sigma$, 10.03σ, and 14.96σ. This selection of pore sizes allowed us to change the ratio of the pore to nanoparticle size between 2.54 and 7.48. Each pore was 29.4σ deep. The pore wall had the same surface charge density as a substrate. The solvent was treated implicitly as a medium with the dielectric permittivity ε. The electrostatic interactions between all charges in a system were taken into account explicitly through the Coulomb potential. The value of the Bjerrum length was set to $l_B = 1.0\sigma$, where $l_B = e^2/\varepsilon k_B T$ is defined as the length scale at which the Coulomb interaction between two elementary charges e, in a medium with the dielectric constant ε, is equal to the thermal energy $k_B T$. In aqueous solutions at room temperatures $T = 300$ K, the value of the Bjerrum length is equal to $l_B = 7.14$ Å. To model L-b-L assembly of charged nanoparticles on porous substrates we have performed 10 sequential molecular dynamics simulations of the adsorption of positively and negatively charged nanoparticles from solutions of nanoparticles. The simulation details of the L-b-L deposition procedure and interaction parameters used for these simulations are discussed in the section Model and Simulation Details.

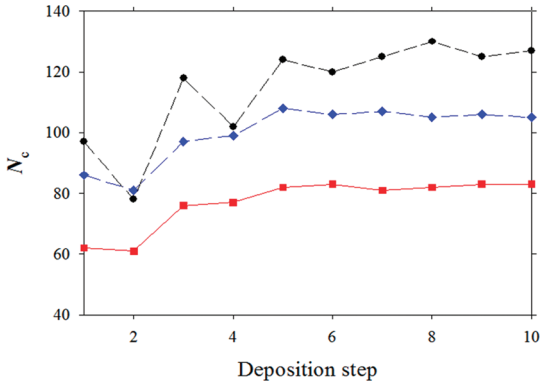

Figure 2. Number of nanoparticles in contact with substrate, N_c, as a function of the number of deposition steps for substrates with different pore sizes: $R_{pore} = 5.09\sigma$ (squares), $R_{pore} = 10.03\sigma$ (rhombs) and $R_{pore} = 14.96\sigma$ (circles).

Film Structure on the Substrate. In Figure 1 we show the evolution of the film structure during deposition steps from 1 through 10 (oppositely charged nanoparticles were adsorbed on the porous charged substrate in a series of consecutive deposition steps). Nanoparticles deposited during different deposition steps are displayed in different colors. The negatively charged nanoparticles adsorbed on the substrates with the pore sizes

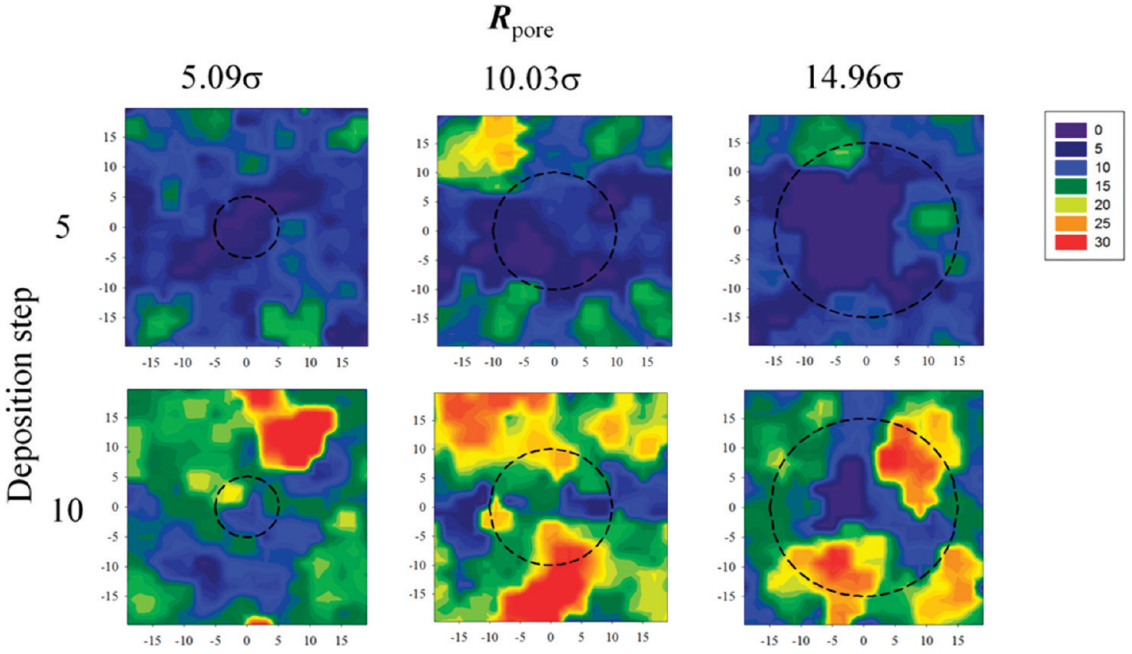

Figure 3. Film height distributions after completion of the fifth and tenth deposition steps for substrates with different pore size. Dashed lines show the pore boundary.

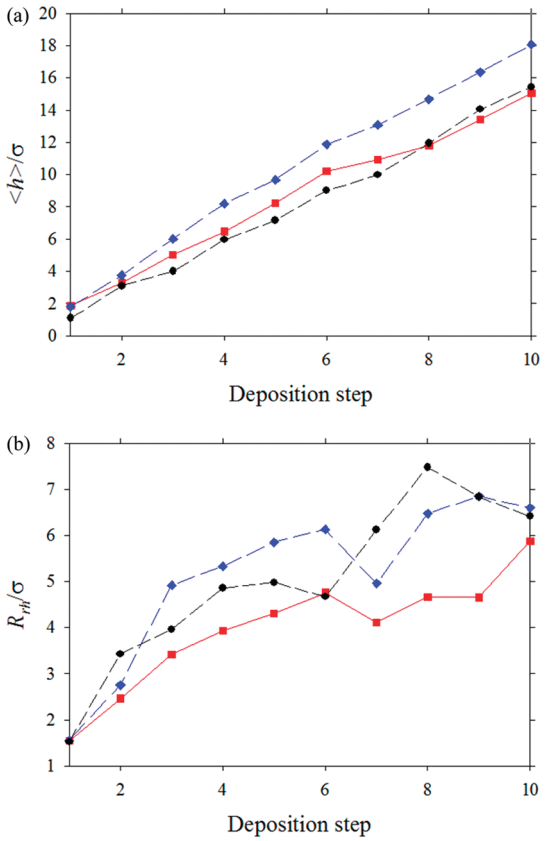

Figure 4. Evolution of the average film thickness $\langle h \rangle$ (a) and the film roughness R_{rh} (b) with the number of deposition steps for substrates with different pore sizes: $R_{pore} = 5.09\sigma$ (squares), $R_{pore} = 10.03\sigma$ (rhombs), and $R_{pore} = 14.96\sigma$ (circles).

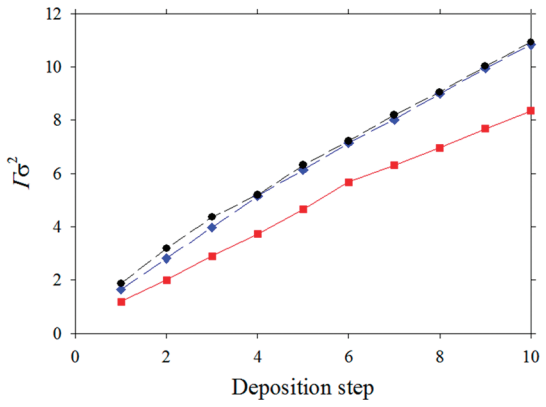

Figure 5. Surface coverage Γ, defined as a number of adsorbed beads per unit area, as a function of the number of deposition steps for substrates with different pore sizes: $R_{pore} = 5.09\sigma$ (squares), $R_{pore} = 10.03\sigma$ (rhombs), and $R_{pore} = 14.96\sigma$ (circles).

R_{pore} = 5.09σ and 10.03σ during the first deposition step are arranged into an almost perfect hexagonal lattice (in our simulations, the substrate is positively charged). For these substrates the pore is not large enough to influence the distribution of the nanoparticles in the space between the pores. However, for the system with the largest pore, $R_{pore} = 14.96\sigma$, the presence

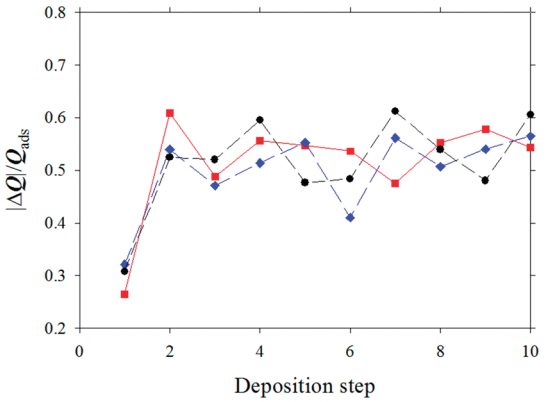

Figure 6. Overcharging fraction as a function of the number of deposition steps for substrates with different pore sizes: $R_{pore} = 5.09\sigma$ (squares), $R_{pore} = 10.03\sigma$ (rhombs) and $R_{pore} = 14.96\sigma$ (circles).

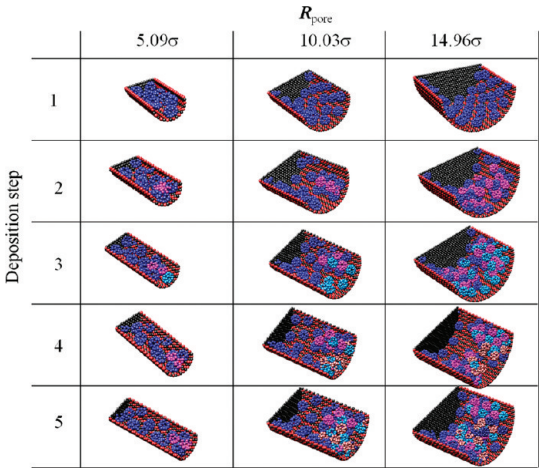

Figure 7. Evolution of the multilayer assembly inside pores. Snapshots are taken after completion of the deposition steps 1−5. The positively charged beads of the substrate are shown in red, and neutral beads are colored in black. The nanoparticles deposited during different deposition steps are shown in different colors: blue (1), magenta (2), dodger blue (3), chestnut (4), and dark blue (5).

of pore begins to influence the nanoparticle distribution (detailed discussion of the layer build up inside the pore is given below). Deposition of the positively charged nanoparticles during the second deposition step alters the structure of the surface layer. For all systems, positively charged nanoparticles form complexes with negatively charged ones by forming strings of negatively and positively charged nanoparticles and exposing the original substrate. This aggregation of oppositely charged nanoparticles optimizes the strong electrostatic interactions between them. Also, the strings of nanoparticles start to cover the pores. In particular, for the substrate with a pore size $R_{pore} = 14.96\sigma$, the strings of oppositely charged nanoparticles make a bridge connecting two opposite sides of the pore. As the film buildup proceeds further, the newly adsorbing nanoparticles first cover the substrate and then start building up a new layer on top of the previously

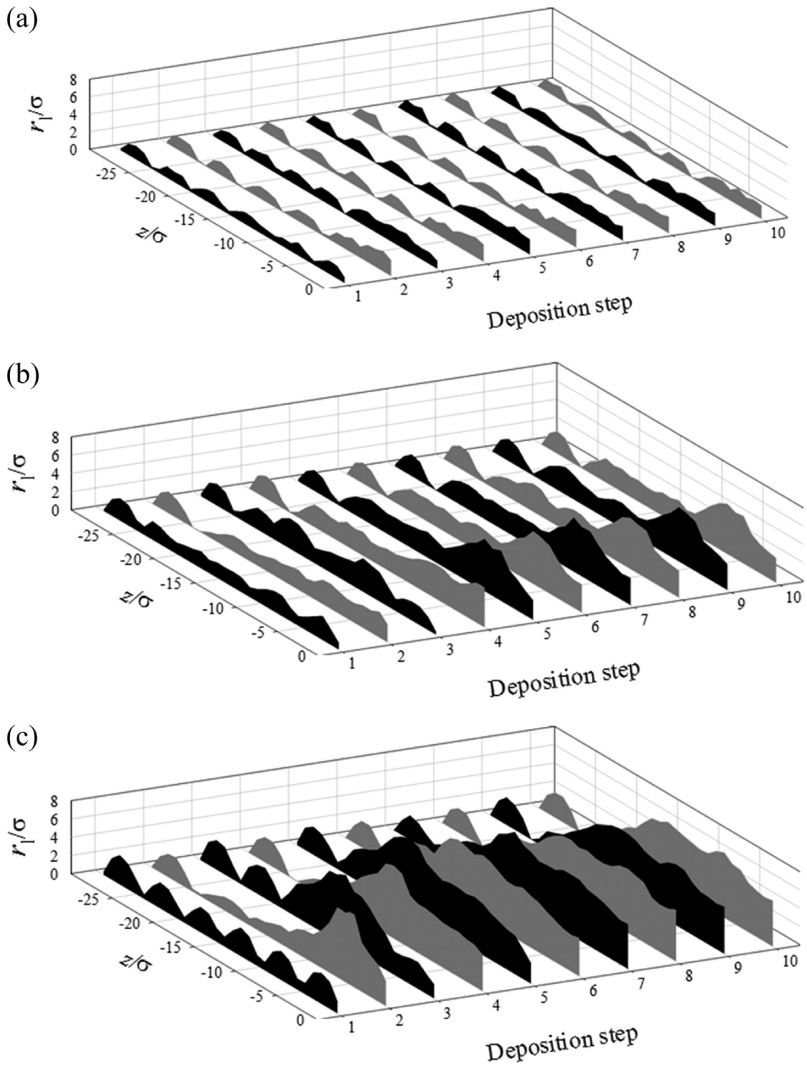

Figure 8. Film thicknesses inside pore r_l as a function of the pore depth z obtained during different deposition steps for substrates with pore sizes $R_{pore} = 5.09\sigma$ (a), $R_{pore} = 10.03\sigma$ (b), and $R_{pore} = 14.96\sigma$ (c).

assembled ones. The pores are slowly closing as more and more nanoparticles aggregate. The smallest pore with a radius 5.09σ is completely closed after completion of the second deposition step. However, it requires six deposition steps to cover a pore with radius 10.03σ. Our largest pore remains open after completion of the ten deposition steps. The reorganization of the film structure can be followed by monitoring the number of nanoparticles in direct contact with the substrate N_c (see Figure 2). In every odd deposition step, negatively charged nanoparticles adsorb onto the surface resulting in an increase of the number of nanoparticles in contact with the substrate N_c. The decrease of the number of nanoparticles in contact with the substrate during the even deposition steps indicates that nanoparticles desorb in pairs. This optimizes the gain of electrostatic attraction between nanoparticles upon aggregation.[19] With increasing the number of deposition steps, the number of nanoparticles in contact with substrate saturates. This saturation supports the observation that at later stages of the deposition process the film grows through the formation of the layer of nanoparticles at the film edge.

The presence of pores influences the film topography. To quantify the effect of the pore size on the film topography, we utilized the bead height sorting algorithm which selects a bead located at the furthest distance from the substrate for each bin in the 40×40 array that covers the surface. For this array size the bin size is approximately equal to $\sigma \times \sigma$. The 2-D contour plot of this 40×40 matrix gives a local film height distribution that provides information similar to the atomic force microscopy (AFM) measurements. All topographic images shown in Figure 3 were obtained using the last configurations of the fifth and tenth deposition step simulations. The snapshots of these configurations are shown in Figure 1. The topographic images also confirm our observation that the largest pore remains open during the entire deposition process.

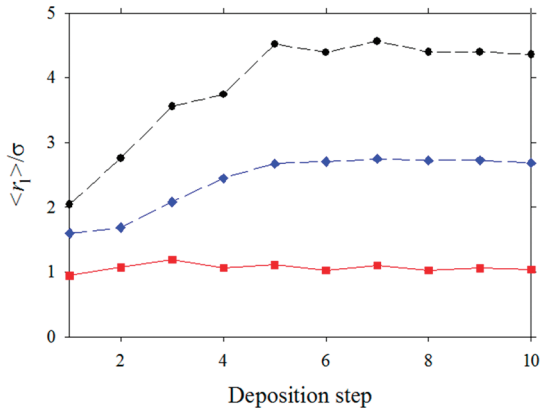

Figure 9. Average film thicknesses inside pore $\langle r_l \rangle$ as a function of the number of deposition steps for substrates with different pore sizes: $R_{pore} = 5.09\sigma$ (squares), $R_{pore} = 10.03\sigma$ (rhombs), and $R_{pore} = 14.96\sigma$ (circles).

The average thickness of the layer $\langle h \rangle$ was calculated as the average value of the height distribution, and the film roughness was obtained from the second moment of this distribution

$$R_{rh} = \sqrt{\langle N_{bin}^{-1} \sum_i (h_i - \langle h \rangle)^2 \rangle} \quad (1)$$

where N_{bin} is the number of bins. These quantities were taken from the last configuration of the each deposition step. Figure 4 panels a and b show the evolution of the average film thickness $\langle h \rangle$ and the film roughness with the number of deposition steps. The film thickness increases with increasing the number of deposition steps for all substrates independent of the pore size. The largest film thickness increase is observed for the substrate with an intermediate pore size. However, the substrates with smallest and largest pore sizes have similar values of film thickness. This film thickness dependence could be a result of the heterogeneous substrate coverage by nanoparticles. The large fluctuations in the height distribution are further corroborated by the large values of the film roughness seen in Figure 4 b.

The surface coverage Γ, defined as the number of adsorbed beads per unit area, monotonically increases with increasing number of deposition steps (see Figure 5). The linear growth corresponding to the steady state regime is observed after completion of the first couple deposition steps. The surface coverage shows slightly faster increase for films growing at the substrates with larger pore sizes. This can be explained by the additional adsorption of nanoparticles within the pores. However, with increasing the number of deposition steps, this difference diminishes indicating that the hole in the film formed by the pore is slowly filled with nanoparticles. Note that for our smallest pore the surface coverage is always smaller in comparison with that for substrates with $R_{pore} = 10.03\sigma$ and 14.96σ. For such a narrow pore, the pore is closed by the adsorbing

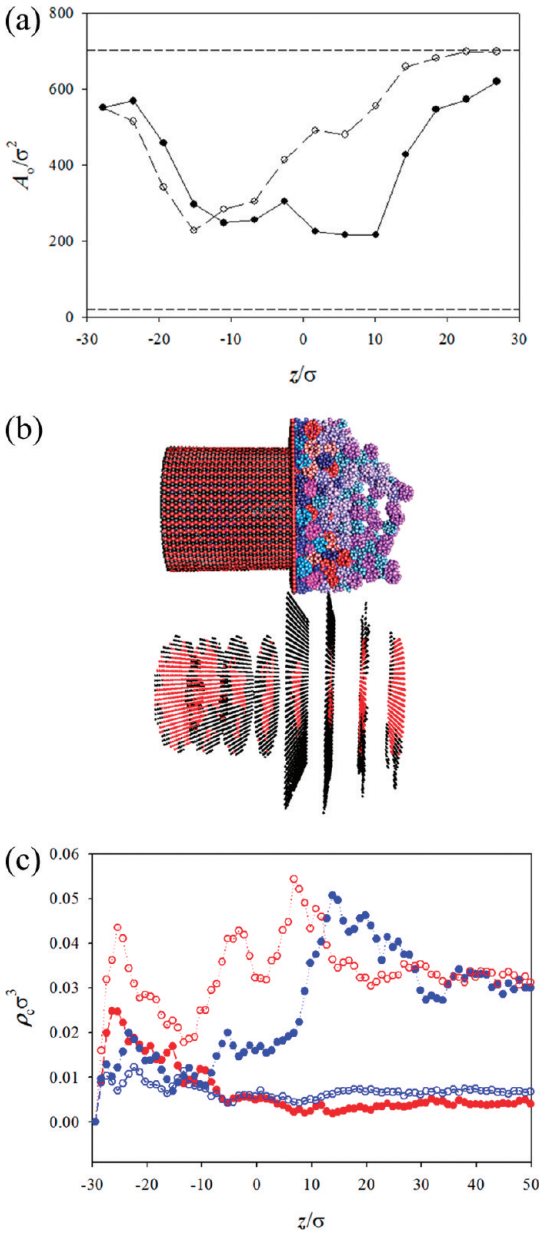

Figure 10. (a) Dependence of the effective open area of a pore A_o along the z-axis with pore size $R_{pore} = 14.96\sigma$ after completion of the fifth (open circles) and tenth (filled circles) deposition steps. The dashed lines show cross section areas of an original pore (top line) and a nanoparticle (bottom line). (b) Distribution of the open pore space along z-axis after completion of the tenth deposition step and snapshot of the multilayer film. (c) Density distribution of small ions along z-axis inside a pore obtained during the fifth (open circles) and the tenth (filled circles) deposition steps. Density distribution of positive and negative ions is shown by red and blue symbols, respectively.

nanoparticles after completion of the second deposition step (see Figure 3). After the pore is closed the film growth demonstrates features similar to the ones observed for multilayer deposition at substrates without the pores.[18−20]

The substrate overcharging during film growth is shown in Figure 6, where the ratio of the absolute value of the film overcharging $|\Delta Q|$ (excess of the positively

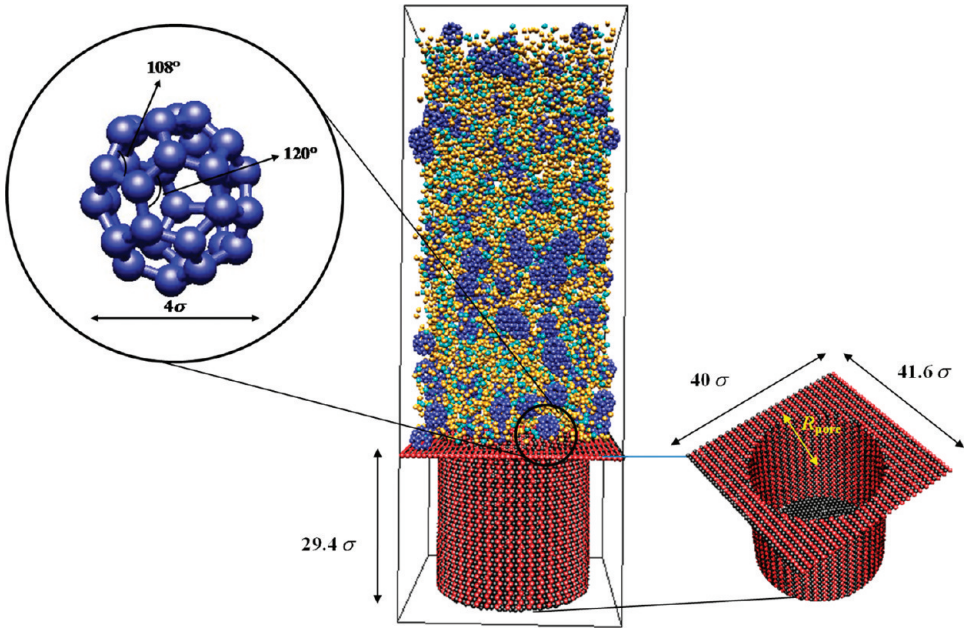

Figure 11. Snapshot of the simulation box. Blue nanoparticles and cyan counterions are negatively charged, red surface atoms and orange counterions are positively charged, and neutral substrate particles are colored in black. Insets show C32 fullerene-like nanoparticle and a substrate with cylindrical pore.

or negatively charged beads including those belonging to the substrate within growing film at a given deposition step) to the absolute value of the total charge $Q_{ads} = 32N_{ads}(s)$ carried by all nanoparticles $N_{ads}(s)$ adsorbed during the sth deposition step. This quantity approaches a value of 0.5 with the increasing number of deposition steps. A similar trend was observed in all our simulations of the multilayer assembly process[16−19] and can be explained as follows. For a steady state growth, half of the adsorbed nanoparticles is used for neutralization of the film excess charge, while the other half recreates the film charge necessary for the adsorption of the next layer. If this ratio is smaller than 0.5, the film eventually stops growing. However, if it exceeds 0.5, the surface coverage will show an exponential growth. In both cases, the growth process is unstable. Thus, the surface overcharging rebuilds the surface properties for the next deposition layer and prevents the unrestricted growth of the adsorbed amount, which is stabilized by the electrostatic repulsions between the excess charges.

Layer-by-Layer Assembly inside Pores. In this section we will discuss structure of the L-b-L film inside a pore. Figure 7 combines snapshots of the layer structure after completion of the deposition steps from 1 through 5. During the first deposition step nanoparticles adsorbed on a pore wall arrange into a set of rings. On each ring nanoparticles are equally spaced along the ring circumference. Two neighboring rings are rotated with respect to each other by an angle equal to the half of the angular distance between nanoparticles such that a nanoparticle faces an empty space on the neighboring rings. For large pores such particle

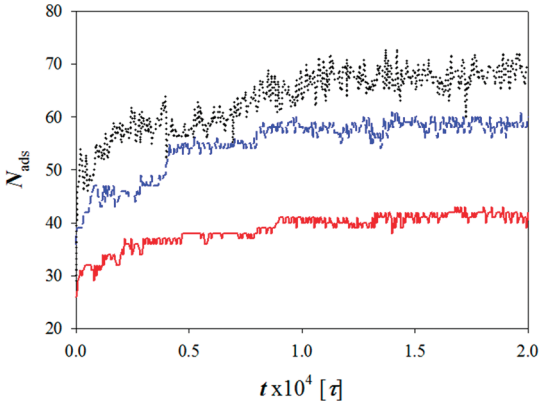

Figure 12. Evolution of the number of adsorbed nanoparticles on substrates with different pore sizes: $R_{pore} = 5.09\sigma$ (solid line), $R_{pore} = 10.03\sigma$ (dashed line) and $R_{pore} = 14.96\sigma$ (dotted line).

arrangement results in a hexagonal pattern on the surface of the cylindrical pore. This layered structure minimizes electrostatic repulsion between nanoparticles. The discrete particle placement can be seen in Figure 8 showing the height distribution along the pore. During the second deposition step newly adsorbed nanoparticles disrupt the layer structure at the pore entrance (see Figures 7 and 8) while the structure of the layer deep inside the pore is preserved. As the deposition process proceeds further the nanoparticles mostly coagulate at the pore entrance thus creating an effective plug preventing newly adsorbing nanoparticles from penetrating deep into the pore. Our smallest pore was closed after completion of the second deposition step. After that the structure of the layer inside

the pore remains the same (see Figure 7 and 8). For the intermediate pore size the layer rearrangements continue throughout the first five deposition steps and after that the particle distribution inside the pore is almost unchanged. This is supported by the evolution of the film thickness along the pore seen in Figure 8. The layer structure for the largest pore evolves during the first seven deposition steps with the narrow region growing gradually in size from the cylindrical pore entrance (see Figures 7 and 8).

Experimentally, the evolution of the film structure inside a pore can be monitored by optical waveguides spectroscopy.[39] These measurements provide information about average film thickness inside a pore. In Figure 9, we plot the dependence of the average film thickness inside a pore as a function of the number of deposition steps. For small pores we see a very fast saturation of the film thickness. For the pore of intermediate size the film thickness saturates when the pore is physically closed, such that no new nanoparticles can penetrate through the film opening and reach the cylindrical pore in a substrate. Our largest pore remains open throughout the entire deposition process (see Figure 1); however, the film thickness inside a pore demonstrates a significant increase only during the first five deposition steps. Thus, during these deposition steps the remaining pore opening is sufficiently large in order to allow a newly adsorbing nanoparticle to pass through the opening in the film and penetrate inside the pore. To illustrate this Figure 10 panels a and b show the dependence of the open area of a pore with radius $R_{pore} = 14.96\sigma$ along the z-axis. As one can see, the pore in a film narrows close to the original pore entrance located at $z = 0$. The cross sectional area of the pore decreases with increasing the number of deposition steps, indicating that the nanoparticles penetrate inside the pore and adsorb on its walls. Also, the thickness of the narrow region grows with an increase in the number of deposition steps (see Figure 10a). This tells us that the nanoparticles first adsorb on the pore walls close to its entrance and do not have sufficient time to penetrate deep inside the pore. Since the area of the pore opening is always much larger than the cross sectional area of the nanoparticle, the long-range electrostatic interactions between newly adsorbing nanoparticles and those forming a multilayer film are the main factors hindering nanoparticle diffusion through a pore. To corroborate this observation in Figure 10c we show the distribution of the counterion density along the pore axes during the later stages of the fifth and tenth deposition steps. One can clearly see an increase in the concentration of counterion inside a pore in comparison with that in a bulk solution. The counterion distribution inside a pore is nonmonotonic, reflecting the layered structure of nanoparticle film.

CONCLUSIONS

We have studied the effect of the pore size on the L-b-L assembly of charged nanoparticles on charged substrates. The deposition of the nanoparticles on the substrate has features similar to those observed for L-b-L assembly on regular planar substrates. The film thickness and surface coverage increase almost linear with the number of deposition steps, as expected for steady state film growth. The surface overcharging after each deposition step fluctuates around a half value of the net charge carried by deposited nanoparticles. The amplitude of the charge fluctuations decreases with increasing the number of deposition steps. A qualitatively different behavior is observed for multilayer assembly inside cylindrical pores. In this case, the initial increase in the film thickness is followed by a saturation regime. Note that a similar behavior of film thickness inside cylindrical pores is observed in experiments.[39,45] The saturation in the layer thickness is a manifestation of the narrowing of the pore which inhibits penetration of nanoparticles. The electrostatic interactions play a leading role in this process. The multilayer film formed on the substrate creates an electrostatic trap along the pore axis thus stopping nanoparticles long before they can penetrate deep inside a pore. Furthermore, the layered structure of the film results in a nonmonotonic distribution of counterions inside a pore. The electrostatic control over the nanoparticle penetration depth and pore cross-section area opens possibilities for the application of the L-b-L assembly technique to the preparation of substrates with desired porosity. It is important to point out that the saturation of the film thickness during L-b-L assembly inside pores was also observed during deposition of different nanoparticle/polyelectrolyte pairs[39,45] and can be considered as a general feature of the L-b-L process in confined geometries. We will address this issue in more detail in future publications.

MODEL AND SIMULATION DETAILS

We performed molecular dynamics simulations[46] of the multilayer assembly of oppositely charged nanoparticles on a porous substrate with different pore sizes (see Figure 11). The nanoparticles consisted of 32 charged beads with diameter σ each and had a diameter equal to 4σ. To model charged nanoparticles, we utilized the fullerene C32 structure by rescaling the coordinates of the C-atoms and setting the bond length between them to σ (see inset in Figure 11).[20] The simulation box had the dimensions $L_x \times L_y \times L_z = 40\sigma \times 41.6\sigma \times 110.9\sigma$. The adsorbing positively charged surface was located at $z = 29.9\sigma$ and was modeled by a hexagonally packed lattice of particles with diameter σ. The substrate had a pore with radius equal to $R_{pore} = 5.09\sigma$, 10.03σ, and 14.96σ. The pore was created

by lowering all surface particles inside a circle with radius R_{pore} centered at a point with coordinates (0.0σ, 0.0σ, 29.9σ) to $z = 0.5\sigma$. All surface beads forming the bottom of the pore were neutral. Every second bead belonging to substrate and side walls of the cylindrical pores carried a univalent charge. A pore was 29.4σ deep.

All particles in the system interacted through the truncated-shifted Lennard-Jones (LJ) potential[47]

$$U_{LJ}(r_{ij}) = \begin{cases} 4\varepsilon_{LJ}\left[\left(\frac{\sigma}{r_{ij}}\right)^{12} - \left(\frac{\sigma}{r_{ij}}\right)^{6} - \left(\frac{\sigma}{r_{cut}}\right)^{12} + \left(\frac{\sigma}{r_{cut}}\right)^{6}\right] & r \le r_{cut} \\ 0 & r > r_{cut} \end{cases} \quad (2)$$

where r_{ij} is the distance between ith and jth beads, and σ is the bead diameter chosen to be the same regardless of the bead type. The cutoff distance, $r_{cut} = 2.5\sigma$, was chosen for surface−nanoparticle and nanoparticle−nanoparticle pairs, and $r_{cut} = 2^{1/6}\sigma$, for other short-range interactions. The interaction parameter ε_{LJ} was equal to 0.5 k_BT for nanoparticle−nanoparticle pairs and the interaction parameter ε_{LJ} was set to k_BT for all other pairs, where k_B is the Boltzmann constant and T is the absolute temperature. The choice of parameters for surface−nanoparticle and nanoparticle−nanoparticle LJ-potential corresponds to the effective short-range attraction while interaction potential with $r_{cut} = 2^{1/6}\sigma$ corresponds to pure repulsive interactions.

The connectivity of beads in nanoparticles was maintained by the finite extension nonlinear elastic (FENE) potential[47]

$$U_{FENE}(r) = -\frac{1}{2}k_{spring}R_{max}^{2}\ln\left(1 - \frac{r^2}{R_{max}^{2}}\right) \quad (3)$$

where the spring constant $k_{spring} = 100k_BT/\sigma^2$, and $R_{max} = 1.5\sigma$ is the maximum bond length. The repulsive part of the bond potential was modeled by the truncated-shifted LJ-potential with $r_{cut} = 2^{1/6}\sigma$ and $\varepsilon_{LJ} = k_BT$.

The shape of the nanoparticles was maintained by imposing the harmonic bending potential

$$U_{bend}(\theta) = \frac{1}{2}k_{bend}(\theta - \theta_0)^2 \quad (4)$$

where θ is an angle between two consecutive bonds and the bending constant $k_{bend} = 200k_BT/\text{rad}^2$. The value of the valence angle θ_0 was equal to 108° for pentagons and to 120° for hexagons (see Figure 11).

Interaction between any two charged particles (beads) with charge valences q_i and q_j, and separated by a distance r_{ij}, was given by the Coulomb potential

$$U_{Coul}(r_{ij}) = k_BT\frac{l_Bq_iq_j}{r_{ij}} \quad (5)$$

where $l_B = e^2/\varepsilon k_BT$ is the Bjerrum length, defined as the length scale at which the Coulomb interaction between two elementary charges e, in a dielectric medium with the dielectric constant ε, is equal to the thermal energy k_BT. In our simulations, the value of the Bjerrum length l_B was set to σ. Note that in aqueous solutions at room temperature, $T = 300$ K, the value of the Bjerrum length is equal to $l_B = 7.14$ Å. Counterions from charged surface and nanoparticles were explicitly included in our simulations. All charged particles in our simulations were monovalent ions.

The particle−particle particle−mesh (PPPM) method for the slab-geometry, with the correction term implemented in LAMMPS[47] with the sixth order charge interpolation scheme and estimated accuracy 10^{-5}, was used for calculations of the electrostatic interactions. In this method, the 2-D periodic images of the system are periodically replicated along the z-direction with distance $L = 3L_z$ between their boundaries.

Simulations were carried out in a constant number of particles, volume, and temperature ensemble (NVT) with periodic boundary conditions in the x and y directions. The constant temperature was achieved by coupling the system to a Langevin thermostat.[35] In this case, the equation of motion of ith particle is

$$m\frac{d\vec{v}_i(t)}{dt} = \vec{F}_i(t) - \xi\vec{v}_i(t) + \vec{F}_i^{R}(t) \quad (6)$$

where $\vec{v}_i(t)$ is the bead velocity, and $\vec{F}_i(t)$ is the net deterministic force acting on ith bead of mass m. $\vec{F}_i^{R}(t)$ is the stochastic force with zero average value $\langle\vec{F}_i^{R}(t)\rangle = 0$ and δ-functional correlations $\langle\vec{F}_i^{R}(t)\vec{F}_i^{R}(t')\rangle = 6\xi k_BT\delta(t-t')$. The friction coefficient ξ was set to $\xi = 0.143m/\tau_{LJ}$, where τ_{LJ} is the standard LJ-time $\tau_{LJ} = \sigma(m/\varepsilon_{LJ})^{1/2}$. The velocity-Verlet algorithm with a time step $\Delta t = 0.01\tau_{LJ}$ was used for integration of the equations of motion eq 6.

Simulations of the multilayer assembly were performed by alternating a substrate exposure to solutions of charged nanoparticles. The simulation procedure of the multilayer assembly by sequential deposition of charged nanoparticles was similar to that previously implemented in refs 18−20. At the beginning of the first deposition step, counterions from the charged surface were uniformly distributed over the simulation box. Negatively charged nanoparticles (M_1 =180) consisting of 32 monomers (beads) each, corresponding to monomer concentration above the substrate $c = 0.043\sigma^{-3}$, together with their counterions were then added to the simulation box and the simulation continues until completion of 2×10^6 MD steps. To facilitate nanoparticle adsorption we have performed simulations with stirring steps.[48] In these simulations we have uniformly redistributed the remaining unadsorbed nanoparticles and counterions in the simulation box every 4×10^5 MD steps. Such redistribution forced nanoparticles to refill a depletion zone (the region close to the substrate with low nanoparticle density). The stirring process was very efficient in increasing the surface overcharging at the initial stages of the adsorption process when diffusion of the nanoparticles toward a surface was a limiting step in nanoparticle adsorption. In Figure 12 we show the evolution of the nanoparticle adsorption during the second deposition step.

After completion of the first simulation run ("dipping" step), unadsorbed nanoparticles were removed ("rinsing" step). The unadsorbed nanoparticles were separated from the adsorbed ones by using a cluster algorithm with a cutoff radius equal to 2.0σ [18−20] (the large cutoff distance was selected to ensure the correct identification of the adsorbed nanoparticles). The cluster analysis was performed by analyzing the matrix of distances between all beads in the system. After completion of the simulation run (deposition step), only the counterions needed for compensation of the excess charge of the growing film were kept in the simulation box to maintain electroneutrality of the system.

At the beginning of the second deposition step, the simulation box was refilled with $M_2 = M_1 = 180$ oppositely charged nanoparticles together with their counterions resulting in concentration of newly added nanoparticles to be the same as before, $c = 0.043\sigma^{-3}$. This was followed by the simulation run ("dipping step") lasting another 2×10^6 MD steps. The duration of the each simulation run was sufficient for the system to reach a steady state. We repeated the dipping and rinsing steps to model 10 deposition steps. The final 5×10^5 MD steps were used for data collection. We have increased the simulation box size along the z-direction by the average increment of the layer thickness Δz after each deposition step, starting with the third deposition step. This allowed us to maintain approximately the same volume accessible to nanoparticles on the top of the growing film during the whole deposition process.

Acknowledgment. The authors are grateful to the National Science Foundation for the financial support under the Grant DMR-1004576. The authors would like to express their gratitude to Professor D. Adamson for the critical reading of the manuscript.

REFERENCES AND NOTES

1. Decher, G. Fuzzy Nanoassemblies: Toward Layered Polymeric Multicomposites. *Science* **1997,** *277*, 1232–1237.
2. Kerdjoudj, H.; Berthelemy, N.; Boulmedais, F.; Stoltz, J. F.; Menu, P.; Voegel, J. C. Multilayered Polyelectrolyte Films: A

Tool for Arteries and Vessel Repair. *Soft Matter* **2010,** *6*, 3722–3734.
3. Lutkenhaus, J. L.; Hammond, P. T. Electrochemically Enabled Polyelectrolyte Multilayer Devices: From Fuel Cells to Sensors. *Soft Matter* **2007,** *3*, 804–816.
4. Schonhoff, M. Self-Assembled Polyelectrolyte Multilayers. *Curr. Opin. Colloid Interface Sci.* **2003,** *8*, 86–95.
5. Srivastava, S.; Kotov, N. A. Composite Layer-by-Layer (LBL) Assembly with Inorganic Nanoparticles and Nanowires. *Acc. Chem. Res.* **2008,** *41*, 1831–1841.
6. Sukhishvili, S. A. Responsive Polymer Films and Capsules *via* Layer-by-Layer Assembly. *Curr. Opin. Colloid Interface Sci.* **2005,** *10*, 37–44.
7. Sukhishvili, S. A.; Kharlampieva, E.; Izumrudov, V. Where Polyelectrolyte Multilayers and Polyelectrolyte Complexes Meet. *Macromolecules* **2006,** *39*, 8873–8881.
8. Sukhorukov, G.; Fery, A.; Mohwald, H. Intelligent Micro- and Nanocapsules. *Prog. Polym. Sci.* **2005,** *30*, 885–897.
9. Ariga, K.; Hill, J. P.; Ji, Q. M. Layer-by-Layer Assembly as a Versatile Bottom-up Nanofabrication Technique for Exploratory Research and Realistic Application. *Phys. Chem. Chem. Phys.* **2007,** *9*, 2319–2340.
10. Izquierdo, A.; Ono, S. S.; Voegel, J. C.; Schaaf, P.; Decher, G. Dipping *versus* Spraying: Exploring the Deposition Conditions for Speeding up Layer-by-Layer Assembly. *Langmuir* **2005,** *21*, 7558–7567.
11. Krogman, K. C.; Lowery, J. L.; Zacharia, N. S.; Rutledge, G. C.; Hammond, P. T. Spraying Asymmetry into Functional Membranes Layer-by-Layer. *Nat. Mater.* **2009,** *8*, 512–518.
12. Kolasinska, M.; Krastev, R.; Gutberlet, T.; Warszynski, P. Layer-by-Layer Deposition of Polyelectrolytes. Dipping *versus* Spraying. *Langmuir* **2009,** *25*, 1224–1232.
13. Lefaux, C. J.; Zimberlin, J. A.; Dobrynin, A. V.; Mather, P. T. Polyelectrolyte Spin Assembly: Influence of Ionic Strength on the Growth of Multilayered Thin Films. *J. Polym. Sci., Part B* **2004,** *42*, 3654–3666.
14. Patel, P. A.; Dobrynin, A. V.; Mather, P. T. Combined Effect of Spin Speed and Ionic Strength on Polyelectrolyte Spin Assembly. *Langmuir* **2007,** *23*, 12589–12597.
15. Andres, C. M.; Kotov, N. A. Inkjet Deposition of Layer-by-Layer Assembled Films. *J. Am. Chem. Soc.* **2010,** *132*, 14496–14502.
16. Panchagnula, V.; Jeon, J.; Dobrynin, A. V. Molecular Dynamics Simulations of Electrostatic Layer-by-Layer Self-Assembly. *Phys. Rev. Lett.* **2004,** *93*, 037801–1–4.
17. Panchagnula, V.; Jeon, J.; Rusling, J. F.; Dobrynin, A. V. Molecular Dynamics Simulations of Polyelectrolyte Multilayering on a Charged Particle. *Langmuir* **2005,** *21*, 1118–1125.
18. Patel, P. A.; Jeon, J.; Mather, P. T.; Dobrynin, A. V. Molecular Dynamics Simulations of Layer-by-Layer Assembly of Polyelectrolytes at Charged Surfaces: Effects of Chain Degree of Polymerization and Fraction of Charged Monomers. *Langmuir* **2005,** *21*, 6113–6122.
19. Patel, P. A.; Jeon, J.; Mather, P. T.; Dobrynin, A. V. Molecular Dynamics Simulations of Multilayer Polyelectrolyte Films: Effect of Electrostatic and Short-Range Interactions. *Langmuir* **2006,** *22*, 9994–10002.
20. Jeon, J.; Panchagnula, V.; Pan, J.; Dobrynin, A. V. Molecular Dynamics Simulations of Mutilayer Films of Polyelectrolytes and Nanoparticles. *Langmuir* **2006,** *22*, 4629–4637.
21. Messina, R.; Holm, C.; Kremer, K. Polyelectrolyte Multilayering on a Charged Sphere. *Langmuir* **2003,** *19*, 4473–4482.
22. Messina, R. Polyelectrolyte Multilayering on a Charged Planar Surface. *Macromolecules* **2004,** *37*, 621–629.
23. Abu-Sharkh, B. Stability and Structure of Polyelectrolyte Multilayers Deposited from Salt-Free Solutions. *J. Chem. Phys.* **2005,** *123*, 114907–1–6.
24. Abu-Sharkh, B. Structure and Mechanism of the Deposition of Multilayers of Polyelectrolytes and Nanoparticles. *Langmuir* **2006,** *22*, 3028–3034.
25. Dobrynin, A. V. Theory and Simulations of Charged Polymers: From Solution Properties to Polymeric Nanomaterials. *Curr. Opin. Colloid Interface Sci.* **2008,** *13*, 376–388.
26. Cerda, J. J.; Qiao, B. F.; Holm, C. Understanding Polyelectrolyte Multilayers: An Open Challenge for Simulations. *Soft Matter* **2009,** *5*, 4412–4425.
27. Dobrynin, A. V.; Rubinstein, M. Theory of Polyelectrolytes in Solutions and at Surfaces. *Prog. Polym. Sci.* **2005,** *30*, 1049–1118.
28. Netz, R. R.; Joanny, J. F. Adsorption of Semiflexible Polyelectrolytes on Charged Planar Surfaces: Charge Compensation, Charge Reversal, and Multilayer Formation. *Macromolecules* **1999,** *32*, 9013–9025.
29. Solis, F. J.; de la Cruz, M. O. Surface-Induced Layer Formation in Polyelectrolytes. *J. Chem. Phys.* **1999,** *110*, 11517–11522.
30. Park, S. Y.; Rubner, M. F.; Mayes, A. M. Free Energy Model for Layer-by-Layer Processing of Polyelectrolyte Multilayer Films. *Langmuir* **2002,** *18*, 9600–9604.
31. Shafir, A.; Andelman, D. Polyelectrolyte Multilayer Formation: Electrostatics and Short-Range Interactions. *Eur. Phys. J. E* **2006,** *19*, 155–162.
32. Wang, Q. Modeling Layer-by-Layer Assembly of Flexible Polyelectrolytes. *J. Phys. Chem. B* **2006,** *110*, 5825–5828.
33. Messina, R. Electrostatics in Soft Matter. *J. Phys. Cond. Matter* **2009,** *21*, 113102.
34. Cerda, J. J.; Qiao, B.; Holm, C. Modeling Strategies for Polyelectrolyte Multilayers. *Eur. Phys. J., Spec. Top.* **2009,** *177*, 129–148.
35. Ariga, K.; Ji, Q. M.; Hill, J. P.; Vinu, A. Coupling of Soft Technology (Layer-by-Layer Assembly) with Hard Materials (Mesoporous Solids) to Give Hierarchic Functional Structures. *Soft Matter* **2009,** *5*, 3562–3571.
36. DeRocher, J. P.; Mao, P.; Han, J. Y.; Rubner, M. F.; Cohen, R. E. Layer-by-Layer Assembly of Polyelectrolytes in Nanofluidic Devices. *Macromolecules* **2010,** *43*, 2430–2437.
37. Ding, G. Q.; Yang, R.; Ding, J. N.; Yuan, N. Y.; Shen, W. Z. Microscale Steps and Micro–Nano Combined Structures by Anodizing Aluminum. *App. Surf. Sci.* **2010,** *256*, 6279–6283.
38. Fu, J. P.; Mao, P.; Han, J. Artificial Molecular Sieves and Filters: A New Paradigm for Biomolecule Separation. *Trends Biotechnol.* **2008,** *26*, 311–320.
39. Lazzara, T. D.; Lau, K. H. A.; Abou-Kandil, A. I.; Caminade, A. M.; Majoral, J. P.; Knoll, W. Polyelectrolyte Layer-by-Layer Deposition in Cylindrical Nanopores. *ACS Nano* **2010,** *4*, 3909–3920.
40. Mei, Y. F.; Thurmer, D. J.; Deneke, C.; Kiravittaya, S.; Chen, Y. F.; Dadgar, A.; Bertram, F.; Bastek, B.; Krost, A.; Christen, J.; *et al.* Self-Assembly, and Properties of Ultrathin AlN/GaN Porous Crystalline Nanomembranes: Tubes, Spirals, and Curved Sheets. *ACS Nano* **2009,** *3*, 1663–1668.
41. Popa, G.; Boulmedais, F.; Zhao, P.; Hemmerle, J.; Vidal, L.; Mathieu, E.; Felix, O.; Schaaf, P.; Decher, G.; Voegel, J. C. Nanoscale Precipitation Coating: The Deposition of Inorganic Films through Step-by-Step Spray-Assembly. *ACS Nano* **2010,** *4*, 4792–4798.
42. Roy, C. J.; Dupont-Gillain, C.; Demoustier-Champagne, S.; Jonas, A. M.; Landoulsi, J. Growth Mechanism of Confined Polyelectrolyte Multilayers in Nanoporous Templates. *Langmuir* **2010,** *26*, 3350–3355.
43. Steinhart, M. Supramolecular Organization of Polymeric Materials in Nanoporous Hard Templates. *Adv. Polym. Sci.* **2008,** *220*, 123–127.
44. Alem, H.; Blondeau, F.; Glinel, K.; Demoustier-Champagne, S.; Jonas, A. M. Layer-by-Layer Assembly of Polyelectrolytes in Nanopores. *Macromolecules* **2007,** *40*, 3366–3372.
45. Kim, J. Y.; DeRocher, J. P.; Mao, P.; Han, J.; Cohen, R. E.; Rubner, M. F. Formation of Nanoparticle-Containing Multilayers in Nanochannels *via* Layer-by-Layer Assembly. *Chem. Mater.* **2010,** *22*, 6409–6415.
46. Frenkel, D.; Smit, B., *Understanding Molecular Simulations*; Academic Press: New York, 2002.
47. Plimpton, S. J. Fast Parallel Algorithms for Short-Range Molecular Dynamics. *J. Comp. Phys.* **1995,** *117*, 1–19.
48. Carrillo, J. M. Y.; Dobrynin, A. V. Molecular Dynamics Simulations of Polyelectrolyte Adsorption. *Langmuir* **2007,** *23*, 2472–2482.